Journal of Materials Chemistry A

Elucidating the Mechanism Underlying the Augmented Capacity of MoO2 as an Anode Material in Li-Ion Batteries

Journal:	*Journal of Materials Chemistry A*
Manuscript ID	TA-ART-08-2023-004794.R1
Article Type:	Paper
Date Submitted by the Author:	29-Sep-2023
Complete List of Authors:	Wang, Hua; Indiana University Purdue University at Indianapolis Hao, Wei; University of Texas at Austin, Li, Tianyi; Argonne National Laboratory, X-ray Science Division; Purdue University, Mechanical Engineering Li, Xintong; Indiana University Purdue University Indianapolis Chang, Kai; Indiana University Purdue University at Indianapolis Zhou, Xinwei; Argonne National Laboratory, Centre for Nanoscale Materials; Indiana University Purdue University at Indianapolis, Mechanical and Energy Engineering Hou, Dewen; Boise State University, ; Argonne National Laboratory, Hashem , Ahmed ; National Research Centre, Inorganic Chemistry Hwang, Gyeong; University of Texas at Austin, Chemical Engineering Liu, Yuzi; Argonne national Laboratory, Center for Nanoscale Materials Sun, Chengjun; Argonne National Laboratory Advanced Photon Source Abdel-Ghany, Ashraf; National Research Centre, Inorganic Chemistry El-Tawil , Rasha ; National Research Centre Abuzeid, Hanaa; National Research Centre, Inorganic Chemistry Abbas, Somia; National Research Centre Mullins, Charles; University of Texas at Austin, Department of Chemical Engineering Julien, Christian; Sorbonne Université Zhu, Likun; Indiana University–Purdue University Indianapolis, Department of Mechanical and Energy Engineering

Elucidating the Mechanism Underlying the Augmented Capacity of MoO_2 as an Anode Material in Li-Ion Batteries

Hua Wang[1,2], Wei Hao[3], Tianyi Li[4], Xintong Li[1], Kai Chang [1], Xinwei Zhou[5], Dewen Hou[5], Ahmed M. Hashem[6], Gyeong S. Hwang[3], Yuzi Liu[5], Cheng-Jun Sun[4], Ashraf E. Abdel-Ghany[6], Rasha S. El-Tawil[6], Hanaa Abuzeid Mohamed[6], Somia M. Abbas[6], C. Buddie Mullins[3], Christian M. Julien[7] and Likun Zhu[1]

[1]Department of Mechanical and Energy Engineering, Indiana University Purdue University Indianapolis, Indianapolis, IN 46202, USA
[2]School of Mechanical Engineering, Purdue University, Indianapolis, West Lafayette, IN 47907, USA
[3]Departments of Chemical Engineering and Chemistry, University of Texas at Austin, TX 78712, USA
[4]Advanced Photon Source, Argonne National Laboratory, Lemont, IL 60439, USA
[5]Center for Nanoscale Materials, Argonne National Laboratory, Lemont, Illinois 60439, USA
[6]National Research Centre, Inorganic Chemistry Department, 33 El Bohouth St., (former El Tahrir St.), Dokki-Giza 12622, Egypt
[7]Institut de Minéralogie, de Physique des Matériaux et Cosmologie (IMPMC), Sorbonne Université, UMR-CNRS 7590, 4 Place Jussieu, 75752, Paris, France

Abstract

Transition-metal oxide anode materials have been observed to possess an intriguing surplus of capacity beyond the expected values based on conversion reaction. However, the mechanisms behind this phenomenon have remained contentious and elusive. This study focuses on synthesized nanosized molybdenum dioxide and its electrochemical performance as an anode material for Li-ion batteries. Our findings reveal a substantial increase in capacity upon cycling, achieving approximately 1688 mAh g^{-1}, nearly double the theoretical capacity, after 700 cycles at a 1C rate. To elucidate the mechanisms underlying this augmented capacity, a comprehensive analysis employing *in-situ* and *ex-situ* X-ray diffraction, X-ray absorption spectroscopy, scanning electron microscopy, and transmission electron microscopy was conducted at various stages of the Li-ion cell cycling. Our results indicate that no conversion reaction occurs during the initial discharge phase, with Li_2O and Mo remaining undetected. Instead, $Li_{0.98}MoO_2$ is generated upon lithiation. Further material characterizations employing electron energy loss spectroscopy and energy-dispersive X-ray spectroscopy on the cycled electrode suggest the potential formation of a metallic Li-rich layer at the interface of the Li-ion intercalated phase subsequent to the formation of $Li_{0.98}MoO_2$, contributing to the surplus Li storage. Moreover, electrochemical impedance spectroscopy coupled with *ex-situ* SEM and TEM analyses reveals that alterations in particle size

and morphology, along with changes in the solid electrolyte interphase (SEI) resistance, are instrumental in the capacity variation observed upon cycling.

Keywords: molybdenum dioxide; extra capacity; Li-ion battery; Li-rich phase; *in-situ* characterization

1. Introduction

Li-ion batteries (LIBs) have been widely used in electric vehicles and mobile electronic devices, attributed to their high energy density and long cycle life [1]. To meet the growing demand for extended driving ranges in electric vehicles and prolong the stand-by time for portable electronic devices, it is imperative to augment the energy density of LIBs, which is determined by the voltage of the LIB and the capacity of LIB electrode materials, including both the anode and cathode.[2, 3] Anode materials are mainly based on four fundamental storage mechanisms: intercalation, conversion reactions, alloying reactions, and Li plating and stripping. Amongst these, the graphite anode, based on intercalation, is the sole anode material that has reached a level of maturity and safety for commercial LIBs. However, graphite anodes are hampered by a relatively low capacity (372 mAh g^{-1}).[4] Recently, transition-metal oxide (TMO) anodes based on conversion reactions have emerged as promising candidates for LIBs due to their high theoretical capacity, low cost and safety.[5-12] The conversion reaction between Li ion and transition-metal oxides is shown in the following equation:

$$M_xO_y + 2yLi^+ + 2ye^- \leftrightarrow xM^0 + yLi_2O \ (M = transiton\ metal). \quad (1)$$

According to the above equation, $\frac{2y}{x}$ Li ions can be stored per metal atom.[13] Following the discovery of this conversion reaction-based anode in 2000, Tarascon et al. observed an interesting phenomenon, wherein an additional reversible capacity, ranging from 0.5 to 0.7 Li per metal atom and exceeding the theoretical limit as per the conversion reaction manifested [14-16]. Since then, similar extra capacity has been discovered in many TMO anode materials including MnO, Fe_2O_3, Fe_3O_4, CoO, NiO, CuO, and MoO_2.[17-29]. The extra Li storage capacities generally surpass the theoretical capacity by 10-100% [30]. Various mechanisms have been postulated to elucidate the origins of the additional capacity exhibited by TMO anodes. Tarascon's group attributed the extra capacity of CuO and CoO to the formation of a polymer/gel-like film during cycling, which grows at low potential and disappears at high potential.[31, 32] Later on, the extra capacity was ascribed to

interfacial charge storage that occurs between metal nanocrystals and Li salts.[33-37]. Furthermore, Grey et al. proposed that the primary contribution to the extra capacity in a RuO_2 anode was the generation of LiOH and its subsequent reversible reaction with Li to yield Li_2O and LiH. Recently, Yu et al. employed *in-situ* magnetometry to investigate the evolution of the internal electronic structure in Fe/Li_2O nanocomposites, with the objective of unravelling the origin of the extra capacity in the Fe_3O_4 anode.[38] Their findings revealed that electrochemically reduced Fe nanoparticles possess the ability to store an abundance of spin-polarized electrons in Fe_3O_4/Li model battery systems during low-voltage discharge, which results in a large excess capacity and a pronounced change in the interface magnetization. Moreover, they verified the existence of such capacitance in CoO, NiO, FeF_2, and Fe_2N electrode materials.

In addition to the mechanisms governing the extra capacity, a diverse array of capacity variation patterns accompanied by extra capacity upon cycling has been documented in the literature.[39] Within the scope of TMO anode materials, the evolution of capacity with cycling can be categorized into four patterns. The first pattern, termed as the "mound-shaped" variation, is characterized by an initial increase in capacity followed by a subsequent decline. This pattern is predominantly manifested in anode materials composed of cobalt oxides.[32, 40] The second category, designated as the “upward-shape”, is exemplified by an Mo-oxide electrode, wherein the capacity increases continuously upon cycling.[41] The third class of capacity variation is labeled as the "U-shaped" pattern. This is in stark contrast to the mound-shaped variation. In this pattern, the capacity initially exhibits a decrease, followed by an augmentation in subsequent cycles. This behavior has been observed in certain Mo-oxide materials.[42, 43] The final category, denoted as the “stable pattern”, is typified by a virtually unchanging capacity upon cycling. Anode materials such as iron oxide and molybdenum oxide are illustrative examples of this category.[44, 45]

Within the spectrum of metal oxides, molybdenum dioxide (MoO_2) emerges as a promising anode material for LIBs. This is predominantly attributable to its distinct layered crystalline structure, which is highly conducive to the intercalation and de-intercalation of Li ions. In conjunction with this favorable structural configuration, MoO_2 boasts an array of advantageous properties encompassing metal-like conductivity (~6×10^3 S cm^{-1}), low toxicity, cost-effectiveness, and robust chemical and thermal stability. Moreover, MoO_2 has a density of 6.5 g cm^{-3}, endowing it with a

theoretical capacity of 838 mAh g^{-1}. This is over twice the capacity of traditional graphite, rendering it a superior alternative for energy storage applications [46-50]. Notably, there has been an increasing emphasis on nanoscale MoO_2, as materials at this scale generally exhibit enhanced properties. Researchers have synthesized various morphologies of MoO_2 to augment its electrochemical performance.[47, 48, 51, 52] Recently, there has been a growing interest in the puzzling phenomenon of excess capacity displayed by nanosized MoO_2 electrodes, whereby MoO_2 exhibits a capacity exceeding its theoretical value based on the conversion reaction principle. In 2022, Wei et al. presented a groundbreaking study in which they synthesized a composite anode material comprising graphene sheets and nitrogen-phosphorus (N-P) co-doped carbon-coated MoO_2. Remarkably, this composite delivered a specific capacity of 1233 mAh g^{-1} at lower current rates, which eclipses the theoretical capacity of MoO_2. The authors posited that MoO_2 served primarily as a conventional material, attributing the surplus capacity to the defects and active sites engendered by N-P co-doping. [53] In contrast, Shon et al. proposed an alternative mechanism to elucidate the high capacity observed in mesoporous MoO_2 material, which was almost double the theoretical limit predicated on the conversion reaction. Employing *in-situ* X-ray absorption, scanning transmission electron microscopy (STEM) complemented with electron energy loss spectroscopy (EELS), and computational modeling, they conjectured that the surplus capacity originated from the formation of a metallic Li-rich phase between the Li ion-intercalated MoO_2 phase.[15] Recently, Alshareef et al. documented an anomalous Li-storage capacity in atomically thin 2D sheets of non-layered MoO_2, exhibiting an astounding 1516 mAh g^{-1} at lower current rates. Through *ex-situ* X-ray photoelectron spectroscopy (XPS) and X-ray diffraction (XRD) analyses, they discerned a Li-storage mechanism entailing an intercalation reaction and the formation of a metallic Li phase within these 2D MoO_2 electrodes.[45] A congruent conclusion was reached by Mai and colleagues, who engineered a MoO_2/carbon (MoO_2/C) hybrid structure with ultrafine MoO_2 nanoparticles ensconced within a carbon nanosheet matrix, achieving a capacity of 896 mAh g^{-1}.[54] In our prior research, we demonstrated that nanosized MoO_2 employed as an anode material manifests an intriguing capacity pattern that approximates twice the theoretical value [55]. This pattern is characterized by an intricate 'W' shape, akin to a combination of U-shape and mount-shape. Upon cycling, the capacity undergoes an initial decline in capacity, followed by an ascent after approximately 10 cycles, another decline post 50 cycles, and eventually a gradual rise.[55] The analysis of capacity variation patterns is imperative for elucidating the underlying determinants

responsible for the enhancement of Li storage, particularly for patterns that demonstrate a capacity increment upon cycling. The purpose of this paper is to provide a mechanistic understanding of the extra capacity and W-shape capacity variation observed in a MoO_2 nanoparticle electrode.

In this study, MoO_2 was synthesized by calcining precursors under a neutral atmosphere (vacuum) at 450 °C. Then the synthesized materials were fabricated into coin cells to analyze their electrochemical properties. Additionally, some samples were fabricated as *in-situ* coin cells for *in-situ* XRD and *in-situ* X-ray absorption spectroscopy (XAS) experiments, which were instrumental in elucidating the reaction mechanisms during cycling. Following these experiments, the coin cells were disassembled to examine the variation in the material by employing *ex-situ* scanning electron microscope (SEM) and *ex-situ* transmission electron microscopy (TEM). Complementary analyses, including selected area electron diffraction (SAED) and electron energy loss spectroscopy (EELS), were conducted to investigate the composition of the electrodes in lithiated and delithiated states. Furthermore, a sequence of electrochemical impedance spectroscopy (EIS) tests was carried out to monitor the variations in the solid electrolyte interface (SEI) resistance throughout the cycling process.

2. Experimental

Materials

Molybdenum dioxide nanoparticles were synthesized via a sol-gel synthesis method using a chelating agent and ammonium molybdate tetrahydrate $(NH_4)_6Mo_7O_{24}.4H_2O$ as the source of molybdenum. Super C65 (conductive carbon black, Timcal Co., Ltd.), polyvinylidene fluoride (PVDF, 12wt%, Kureha Battery Materials Japan Co., Ltd.), 1-methyl-2-pyrrolidinone (NMP, anhydrous 99.5%, Sigma-Aldrich), 1M $LiPF_6$ in ethylene carbonate and dimethyl carbonate solution mixed as 1:1 vol ratio (BASF Corporation), Li ribbon (thickness 0.38mm, 99.9% trace metals basis, Sigma-Aldrich) were purchased and used as received.

Fabrication of electrode

Molybdenum oxides electrodes were fabricated using 5:3:2 (mass ratio) mixture of active material (MoO_2 powder), carbon black (super C65), and binder (PVDF). The mixture was added to NMP

solvent. The mixed slurry was stirred by a magnetic stir bar for 24 h to blend homogeneously. The well blended slurry was cast on a copper foil by a doctor blade, and dried under vacuum at 100℃ for 24 h. The dried electrodes were punched out as ~0.97 cm^2 discs (diameter = 11mm) with 1.4 mg cm^{-2} and transferred into an Ar-filled glovebox for further handling and testing.

Coin cell assembly

The fabrication of cells, specifically CR2032 coin cells, was carried out in an argon-filled glovebox. The process commenced with the positioning of a stainless-steel disc inside the coin cell casing. Next, an electrode was placed on the disc with the copper side facing downwards. Subsequently, 30 µL of electrolyte was delicately dispensed onto the electrode. This was followed by the placement of a Celgard 2400 separator atop the wetted electrode. Another 30 µL electrolyte was then added on top of the separator to ensure proper saturation. Following this, a piece of Li metal was positioned over the separator, and a stainless-steel disc was used to encase the Li metal. To complete the assembly, a spring was inserted beneath the opposite side of the coin cell case to act as a spacer. The cell was then securely crimped to ensure integrity and was removed from the glovebox in preparation for subsequent electrochemical evaluation.

In-situ coin cell assembly

To facilitate X-ray penetration through the CR2032 coin cell casings, the coin cells were modified for *in-situ* experimentation. Holes with a diameter of 2 mm were precision-punched at the center of both the anode and cathode cases. These holes were then sealed with 30 µm-thick Kapton tape, applied to both sides of each case. The stainless-steel discs were similarly punched to create corresponding holes. The assembly process was the same as assembly of coin cell. Once assembled, the cell underwent a crimping process and was then removed from the glovebox for *in-situ* XRD (X-ray Diffraction) and XAS (X-ray Absorption Spectroscopy) experiments.

Electrochemical evaluation

The cells were connected to an Arbin BT2000 battery cycler for evaluation at room temperature. Prior to the cycling process, the cells were initially rested for 30 min. According to the mass of material in the cell, the cells were cycled galvanostatically at C/10 and 1C rate (1C = 838 mA g^{-1} for MoO_2 weight), in a voltage range between 0.01 V and 3.0 V. Cyclic voltammetry (CV) analyses

were performed at room temperature using a BioLogic VSP workstation, in which the potential was set to sweep from open-circuit voltage to 0.01 V and then to sweep back to 3.0 V at a 0.1 mV s^{-1} scanning rate. Electrochemical impedance spectroscopy (EIS) was also conducted by the VSP workstation in the frequency range from 5×10^5 to 0.1 Hz with an amplitude of 5 mV.

Scanning electron microscopy

The electrodes underwent morphological characterization using a JEOL JSM-7800F Field Emission Scanning Electron Microscope (FE-SEM). For a more detailed analysis of the cross-sectional morphology, the electrodes were examined using a ZEISS NVision 40 Focused Ion Beam Scanning Electron Microscope (FIB-SEM).

Transmission electron microscopy

Similarly, the electrodes also underwent morphological characterization through imaging, as well as Selected Area Electron Diffraction (SAED) and Electron Energy Loss Spectroscopy (EELS) analyses. These assessments were conducted using a JEOL JEM-2100F Transmission Electron Microscope (TEM). SAED data analysis was performed by CrysTBox software.[56]

***In-situ* synchrotron XRD**

The synchrotron XRD experiment was executed at the Advanced Photon Source (APS) on beamline 17-BM. The photon source had a wavelength of 0.24114 Å and an energy of 51 keV. The size of the incident beam, which was utilized on the sample, was precisely 500 μm by 500 μm. The experiment was conducted using the transmission mode, where the detector was strategically positioned at a distance of 700 mm from the sample. The scattering intensity was captured using a high-resolution 2D Varex detector, with each pixel measuring 150 μm and the total array consisting of 2880 by 2880 pixels. The 2D diffraction patterns produced by the synchrotron XRD were calibrated employing a standard cerium dioxide (LaB6) sample. Furthermore, the 2D patterns were converted to 1D patterns through the application of GSAS II software.

In-situ synchrotron XAS

X-ray absorption measurements at the Mo K-edge were performed at room temperature at the bending magnet station 20-BM of the APS at Argonne National Laboratory. The electron storage ring operated at 7 GeV with a stored current of 100 mA. The excitation energies were selected with a double crystal monochromator (Si-(111)), which was detuned by 15%, and a harmonic rejection mirror was used to reject the high-energy harmonics. The incident and transmitted beam intensities were monitored using ionization chambers with nitrogen gas. The energy calibration at the Mo K-edge was set by calibrating the inflection point of a Molybdenum foil to 20005 eV.

Quantum mechanical calculation

Density functional theory (DFT) calculations were performed using the Vienna Ab-initio Simulation Package (VASP) [57-59]. The Perdew-Berke-Emzerhof (PBE) [60] generalized gradient approximation (GGA) was employed to calculate the exchange and correlation energy. Fig. S1 depicts the atomic structure of crystalline MoO_2. The 4p, 4d and 5s valence states of Mo atoms and the 2s and 2p valence states of O atoms were treated explicitly and the remaining core electrons were described using the projector augmented wave (PAW) method [61], while the full electron configuration of $1s^2\ 2s^1$ was considered for Li. The electron wavefunctions were expanded using a plane wave basis set with an energy cutoff of 400 eV. Geometry optimizations were performed by fully relaxing all atoms with the conjugate gradient method until the residual forces on constituent atoms became smaller than 1×10^{-2} eV/Å. The Brillouin zone was sampled using a (3×3×3) Monkhorst-Pack mesh [62] in determining the structure and energetics of pristine and lithiated MoO_2, consisting of 4 formula units in each periodic supercell. For each composition, three different samples were constructed and examined, using the same approach as described in Ref. [63]. In slab calculations, only the gamma point was considered for Brillouin zone integration.

3. Results and discussion

The electrochemical properties of MoO_2 nanoparticles were investigated as anode materials for Li-ion batteries by cycling them within a potential range of 0.01-3.0 V *vs*. Li^+/Li. The MoO_2 material exhibited a noteworthy W-shaped pattern in the variation of discharge capacity upon cycling. Fig. 1a displays this cycling performance at a 1C rate, with the five vertices of the W-

shape labeled in Fig. 1a as points (1) through (5). During the first cycle, the MoO_2 nanoparticles delivered a promising initial discharge capacity of 953 mAh g^{-1}. However, this was followed by a sharp decline over the next five cycles, bottoming out at approximately 683 mAh g^{-1}, as seen from point (1) to point (2). Surprisingly, this downward trend reversed, and the capacity steadily climbed to 850 mAh g^{-1} between point (2) and point (3). Post this increment, the capacity experienced a slight dip from point (3) to point (4). Remarkably, from this nadir, a sustained increase was observed, culminating in a capacity of 1688 mAh g^{-1} at point (5). This value is nearly double the theoretical capacity, signifying a breakthrough in performance. Towards the end of the cycling process, the discharge capacity began to exhibit instability.

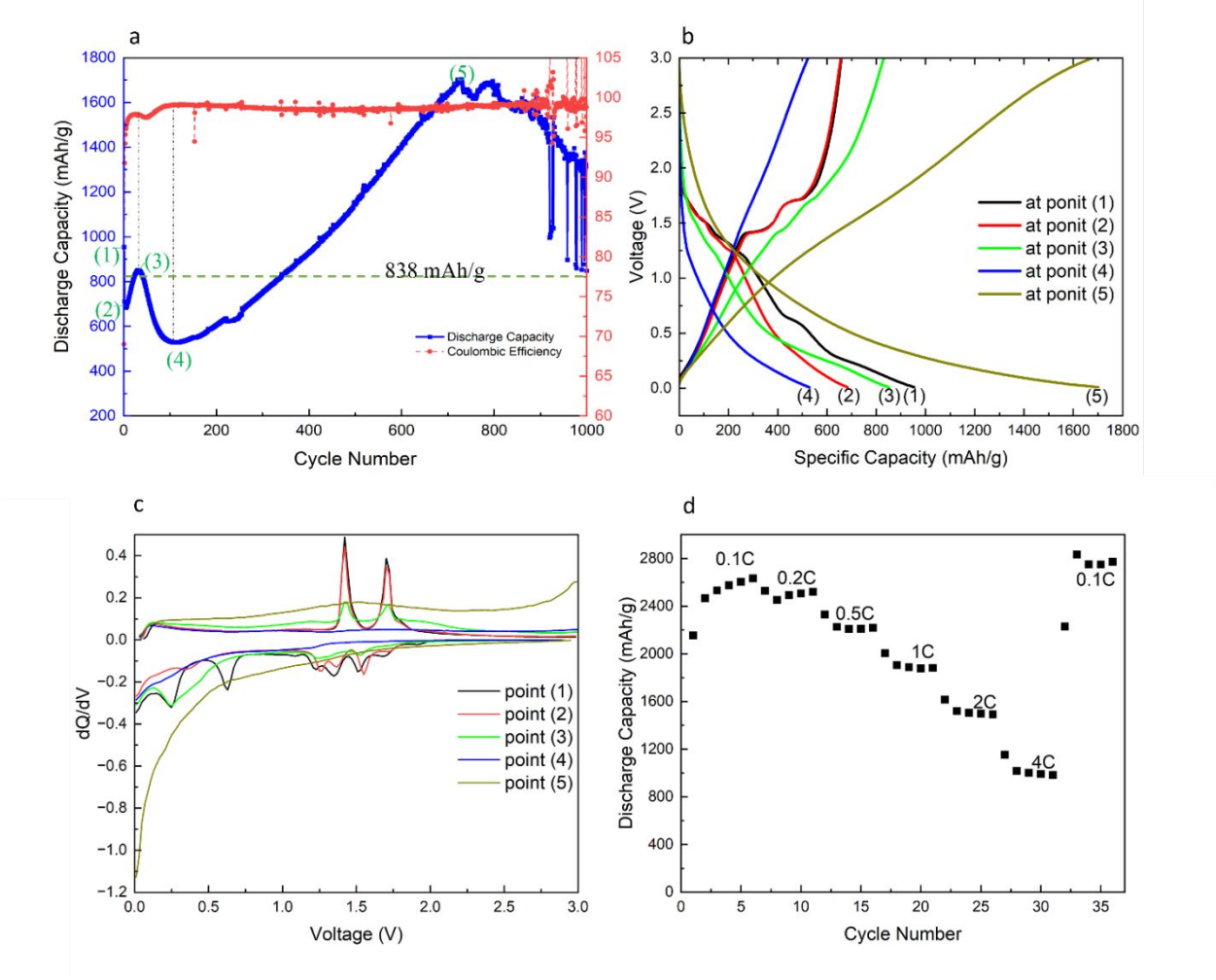

Fig. 1. Electrochemical Performance of MoO_2: (a) Specific Discharge Capacity and Coulombic Efficiency plotted as functions of the number of cycles, measured at a 1C rate; (b) Voltage Profiles at various states of charge/discharge, recorded at a 1C rate within a potential window ranging from

0.01 to 3.0 V *vs*. Li^+/Li; (c) dQ/dV profiles at different cycles carried out at 1C-rate; (d) rate capability of a Li//MoO_2 cycled cell at a cycling point between (4) and (5).

Fig. 1b displays the voltage profiles for cycle points (1) through (5), while Fig. 1c illustrates the corresponding dQ/dV profiles. At cycle point (1), four cathodic peaks are discernible at 0.25, 0.63, 1.25, and 1.55 V *vs*. Li^+/Li, along with two pronounced anodic peaks at 1.43 and 1.70 V. The pairs of peaks at 1.25/1.43 V and 1.55/1.70 V are attributed to the reversible phase transitions, specifically from monoclinic to orthorhombic and back to monoclinic, within the partially lithiated Li_xMoO_2 during Li intercalation (discharge) and deintercalation (charge) processes. Fig. 1c reveals a decline in the intensity of these peaks with cycling, culminating in their complete disappearance at point (4). Beyond this point, the current continues to rise in the dQ/dV profile, but in the absence of any redox reaction peaks. This suggests that the capacity enhancement does not rely on the intercalation mechanism; instead, Li storage seems to align with a capacitive-type charge storage mechanism. The corresponding plateaus in the voltage profiles shown in Fig. 1b exhibit a similar trend. Furthermore, Fig. 1c highlights intriguing changes in the reduction peaks at 0.63 and 0.25 V upon cycling, which warrants further investigation across additional cycling profiles. Video S1 in the supporting information documents the variation of dQ/dV profiles with cycling. The initial cathodic peaks at 0.63 and 0.26 V vanish from the second cycle onwards. This may be ascribed to the reduction of species in the solution and the concomitant formation of a solid electrolyte interphase (SEI). Starting from the second cycle, a stable cathodic peak emerges at 0.34 V, exhibiting a minor shift to 0.25 V through the tenth cycle. Beginning with the eleventh cycle, a prominent cathodic peak at 0.25 V escalates rapidly, peaking at the thirty-eighth cycle, and then diminishes until it vanishes by the one-hundredth cycle (around point 4). It is noteworthy, as depicted in Fig. 1a, that there are two distinct phases in the evolution of Coulombic efficiency (CE) with cycling. Initially, from point (1), CE surges swiftly to 97.3% by the tenth cycle, after which the rate of increase slackens until it reaches 97.9% by the twenty-seventh cycle. However, the escalating SEI cathodic peak not only decelerates the growth rate of CE but also brings about a reduction in CE, which drops to 97.4% by the forty-seventh cycle. Thereafter, up to the one-hundredth cycle (point (4)), CE climbs modestly to around 99.4% and stabilizes. The fluctuations in the dQ/dV peaks corresponding to SEI formation are correlated with the variations in CE.

The enhancement in excess capacity between points (4) and (5) was corroborated by the rate capability test. Fig. 1d illustrates the rate capability of an electrode composed of MoO_2 nanoparticles, which underwent cycling at a 1C rate for a total of 350 cycles and attained a capacity of 1692 mAh g^{-1}. As the C-rate escalated from 0.1C to 4C, there was a decline in the discharge capacity, from nearly 2600 mAh g^{-1} to approximately 983 mAh g^{-1}. Interestingly, when the C-rate was reverted to 0.1C, the discharge capacity also bounced back to roughly 2770 mAh g^{-1}. This value surpasses the capacity observed during the inaugural 0.1C test. Such an augmentation aligns with the pattern of capacity alteration observed between points (4) and (5) as depicted in Fig. 1a.

To investigate the mechanism behind the additional capacity, we conducted *in-situ* XRD experiments to uncover the reaction mechanism within MoO_2 nanoparticle electrodes during the discharge and charge cycles. The *in-situ* XRD patterns of a pristine cell are depicted in Fig. 2, where the cell was cycled at a rate of 0.1C. A comparable pattern was obtained for *in-situ* XRD at a 1 C rate, as presented in Fig. S2. In the initial XRD pattern, the peaks depicted in Fig. 2b at 4.04˚, 5.68˚, 8.08˚, and 9.06˚ are ascribed to the (-111), (-211), (-312), and (013) diffractions of monoclinic MoO_2 (PDF# 00-032-0671, P21/n (14)) respectively, while the peaks positioned at 5.53˚, 6.5˚, and 7.9˚ are attributed to Li. Additionally, the peak situated at 4.11˚ is associated with graphite. As the discharge process proceeds, the MoO_2 diffraction peaks exhibit a shift towards lower angles, suggesting lattice expansion as Li ions intercalate into the MoO_2 structure. When the voltage is discharged below 1 V, a novel pattern emerges with peaks at 3.74˚, 5.31˚, 5.39˚, 7.54˚, 7.74˚, 8.40˚, and 8.52˚. These peaks correspond to the (011), (020), (002), (022), (-222), (031), and (013) planes of the monoclinic $Li_{0.98}MoO_2$ phase (PDF# 01-084-0601, P21/c (14)). As is evident from the magnified view of the pattern in Fig. 2c, the Li-ion intercalation into Li_xMoO_2 goes through two distinct stages as x varies from 0 to 0.98. Initially, the Bragg peak (-111) of the monoclinic MoO_2 exhibits a slight shift until a broad peak emerges, which can be assigned to the orthorhombic Li_xMoO_2 phase with x around 0.63, consistent with reference $0.45 < x < 0.78$.[64] Subsequently, as more Li ions intercalate, the monoclinic phase peak re-emerges and experiences a slight shift, corresponding to $Li_{0.98}MoO_2$ (011). This phase transition aligns with results documented in the literature.[64, 65] Interestingly, even as the discharge process continues, the XRD

pattern retains the prominent peaks of $Li_{0.98}MoO_2$ until the voltage is discharged to 0.01 V. At this juncture, the d-spacing remains constant while the full width at half maximum (FWHM) fluctuates irregularly (refer to Fig. S3). It is noteworthy that no Mo metal or Li_2O phases were detected upon the conclusion of the discharge process.

During the charging process, the peaks of $Li_{0.98}MoO_2$, observed in XRD patterns, still remain stable until 1.5 V. After that, the peaks undergo a shift towards higher angles and exhibit broadening. Remarkably, the XRD pattern reverts to that of MoO_2 diffraction after transitioning from the $Li_{0.98}MoO_2$ peaks. This phenomenon signifies that the multi-step phase transformation (monoclinic-orthorhombic-monoclinic) that occurs during the intercalation of Li ions into the MoO_2 electrode to form Li_xMoO_2 is reversible. Furthermore, the XRD findings suggest that the predominant reaction involving this MoO_2 may not be the theoretical conversion reaction as previously assumed. XRD findings only show the intercalation reaction. Notably, the MoO_2 peaks display a slight broadening and shift towards lower angles upon charging. This behavior indicates that some Li ions become trapped within the material, and there is a reduction in grain size. In conjunction with these observations, our analysis of the dQ/dV curves reveals that two pairs of peaks, attributed to the phase changes in Li_xMoO_2 as the value of x varies ($0 < x < 0.98$), are present. Additionally, these peaks diminish over successive charge-discharge cycles, which is likely due to the trapping of Li ions in each cycle. Intriguingly, the measured capacity (953 mAh g^{-1}) surpasses what would be expected from the lithiated product $Li_{0.98}MoO_2$ (205 mAh g^{-1}) alone. This excess capacity implies that the primary contribution to capacity does not stem from any crystallographic transformation reactions. To corroborate these findings, we conducted a series of *in-situ* XRD experiments with different batches of MoO_2 under various cycling conditions (both 0.1C and 1C). The outcomes across all experiments were consistent, further solidifying the observations and conclusions derived from our study.

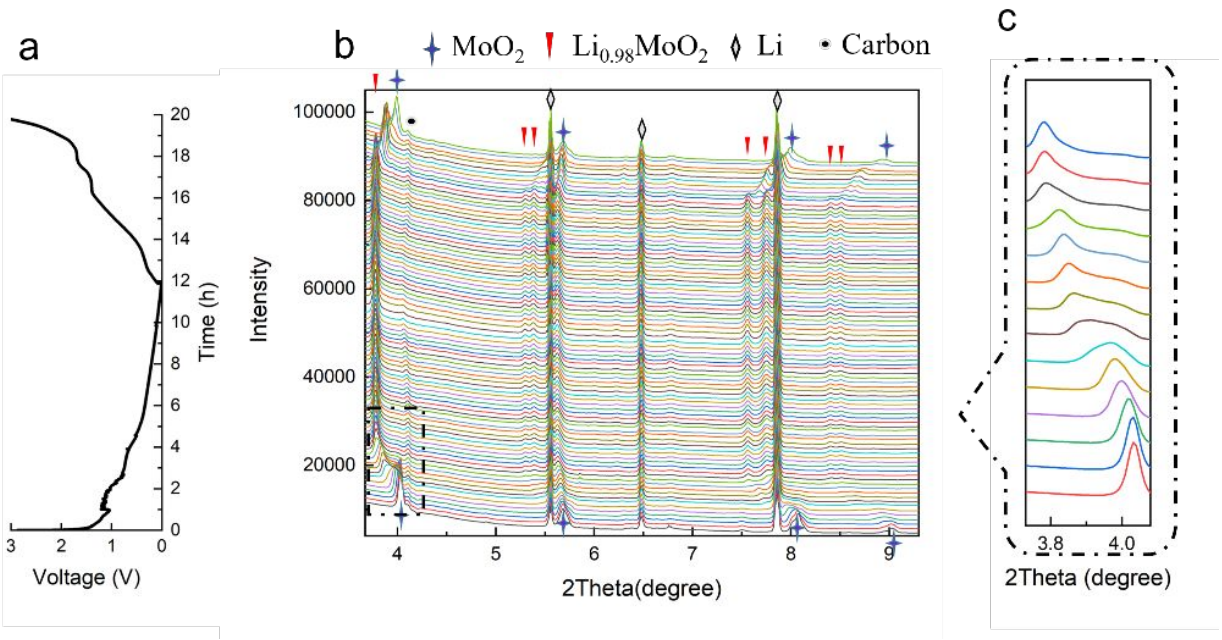

Fig. 2. *In-situ* XRD patterns of a fresh cell at point (1). (a) Voltage profile at a 0.1 C rate during the *in-situ* XRD test; (b) *In-situ* XRD patterns of the fresh cell (at point (1)) operating at a 0.1 C rate; (c) Detailed view of the XRD peaks derived from panel (b).

An *in-situ* X-ray absorption spectroscopy (XAS) experiment was conducted to elucidate the underlying mechanisms. The XAS data revealed three distinct stages during the cycling process. Fig. 3a illustrates the *in-situ* spectroscopy at three different states: the initial state 3 V, after discharging to 0.01 V, and upon recharging to 3 V. The complete in-situ spectroscopy during the first cycling can be found in Fig. S4. Initially, the spectroscopy exhibits a pattern characteristic of Mo^{4+} (MoO_2). As the battery discharges, the Mo K-edge undergoes a shift towards lower energy levels, transitioning from Mo^{4+} (approximately 20009 eV) to a reduced valence state (approximately 20008 eV). Upon recharging, the K-edge almost returns to its original position, indicating a nearly restored Mo^{4+} state. Fig. 3b portrays the *in-situ* XAS data captured during the discharging process, highlighting two markedly different K-edge transitions. Initially, the MoO_2 pattern undergoes a subtle evolution corresponding to the intercalation of Li ions. Below 0.5 V, once $Li_{0.98}MoO_2$ is fully formed, the spectroscopy remains relatively stable with no apparent changes. Upon reaching 0.01 V, the K-edge at 20008 eV significantly deviates from the reference value for Mo in its elemental state, Mo^0 (20005.5 eV), which suggests that the metallic Mo phase

is not present. Moreover, the *in-situ* XAS observations contradict the predictions based on the theoretical conversion reaction.

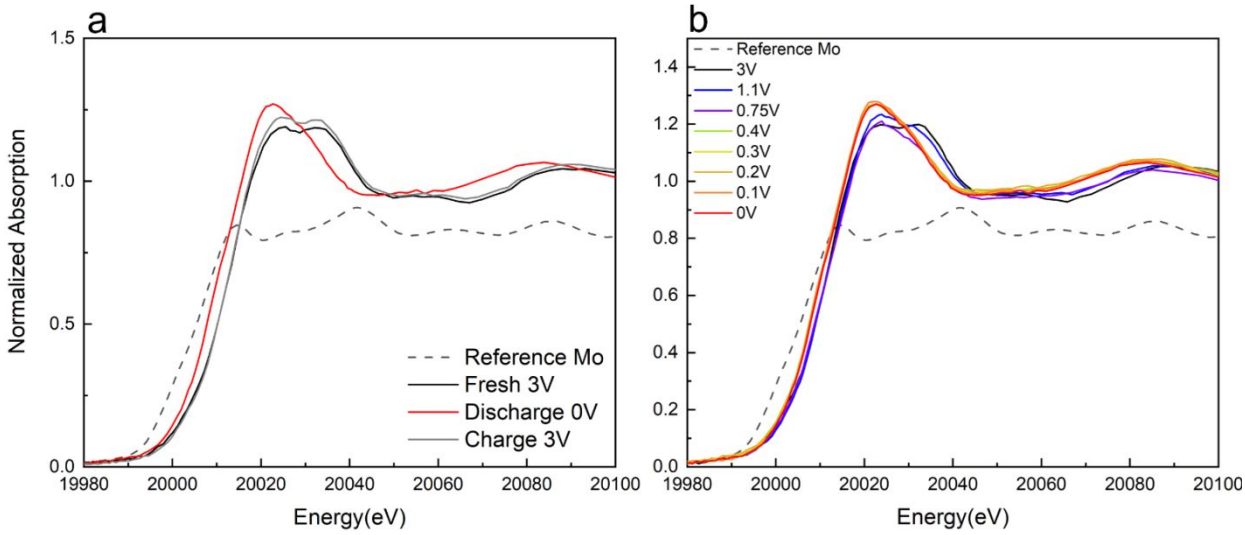

Fig. 3. *In-situ* XAS analysis of a fresh cell at point (1): (a) XAS patterns at initial 3 V, subsequent 0 V, and upon returning to 3 V; (b) XAS patterns observed during the lithiation process.

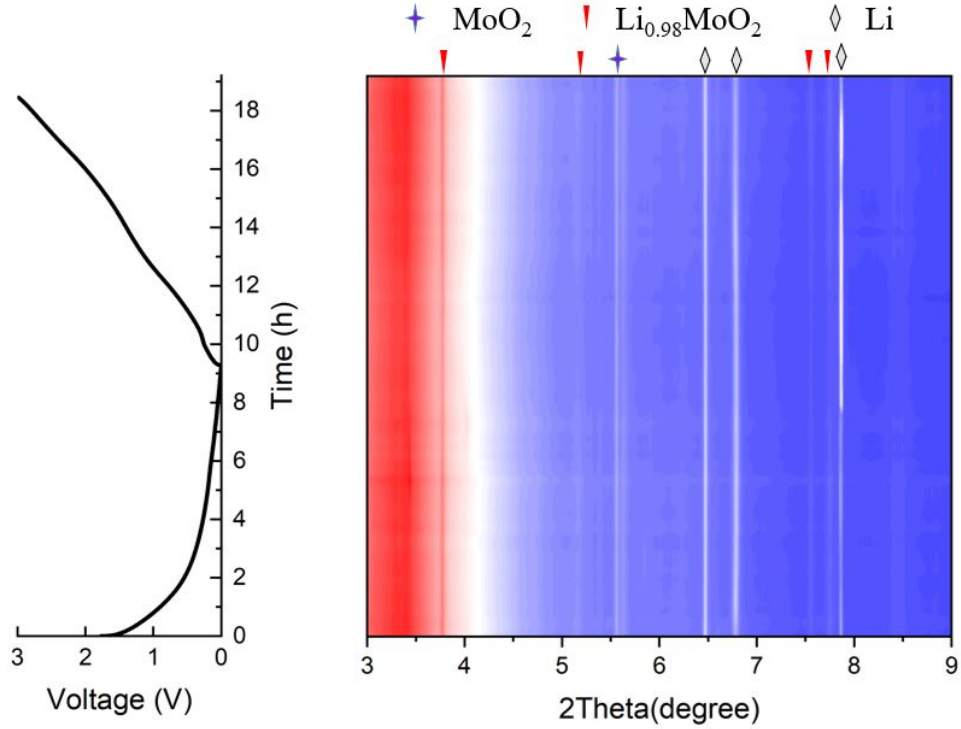

Fig. 4. *In-situ* XRD patterns of a Li//MoO_2 cycled cell at a cycling point between point (4) and (5).

To investigate the Li storage mechanisms that extend beyond theoretical capacity, we conducted *in-situ* XRD experiments. These experiments were performed on a cell that had undergone several hundred cycles and reached a capacity state between points 4 and 5, as depicted in Fig. 4. Notably, the discharge and charge profiles do not exhibit any plateaus. The *in-situ* XRD data reveals that there are no alterations in the crystalline structure throughout the entire discharge and charge cycle. Diffraction peaks can be attributed to MoO_2, $Li_{0.98}MoO_2$, and Li metal. However, these peaks remain unchanged. It is posited that the peak corresponding to Li metal arises from the Li metal reference electrode. Meanwhile, the MoO_2 and $Li_{0.98}MoO_2$ phases can be ascribed to the inactive particles of MoO_2 and $Li_{0.98}MoO_2$ that have become disconnected from the electrical network during the cycling process. Notably, no evidence of the monoclinic-orthorhombic-monoclinic (de)intercalation reactions between MoO_2 and $Li_{0.98}MoO_2$ phases was observed. This could be attributed to the cessation of this reaction or to the possibility that the particle sizes of MoO_2 and $Li_{0.98}MoO_2$ have diminished to such an extent that they are undetectable by XRD. The results from the *in-situ* experiments suggest that the large capacity is a result of a Li storage mechanism that does not involve changes in the crystalline phase. Consistent with the proposition made by Shon et al., it is plausible that the extra capacity originates from a metallic Li-rich phase that forms within the crystalline structure of $Li_{0.98}MoO_2$.[15]

To ascertain the presence of the Li-rich phase, we performed SAED experiments on three distinct samples: pristine MoO_2 nanoparticles, particles post-discharge to 0.01 V, and particles post-charge to 3 V. The particles subjected to discharging and charging processes were extracted from *ex-situ* cells. These cells were meticulously disassembled within a glovebox following the respective discharge and charge cycles. A close examination of the pristine powder (Fig. 5a) and the electrode subsequent to charging at 3 V (Fig. 5c) reveals a diffraction pattern consistent with MoO_2. In contrast, the SAED analysis (Fig. 5b) of the electrode post-discharge at 0.01 V exhibits a diffraction pattern characteristic of $Li_{0.98}MoO_2$. Furthermore, the EELS experiment carried out on the fully discharged electrode is particularly enlightening (Fig. 5d). It unveils the K-edge of metallic Li manifesting at 55 eV [66]. This observation is indicative of additional Li storage, which can be attributed to the metallic Li-rich phase, signifying a storage mechanism beyond the intercalation reaction. Additionally, Fig. S5 presents an EELS analysis of an electrode that's

partially lithiated, with less than 0.98 Li-ions incorporated per MoO_2 molecule. Notably, no metallic lithium was detected at the initial stage of discharging (Li_xMoO_2, $0<x<0.98$).

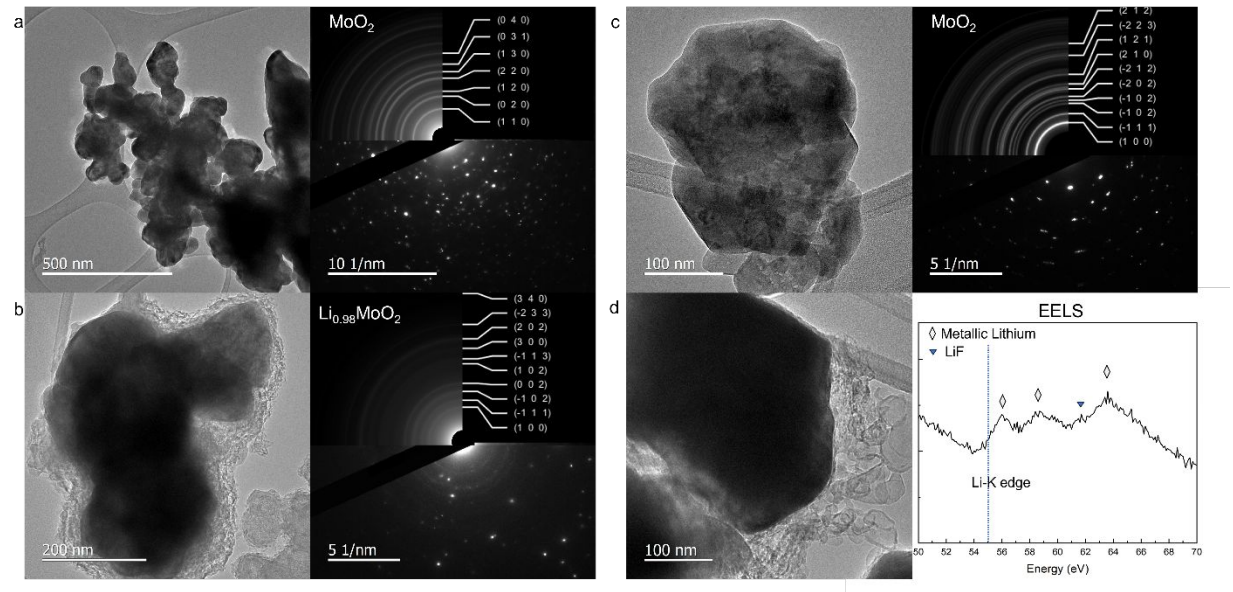

Fig. 5. (a) Bright field TEM image and experimental SAED of pristine powder with indexed MoO_2 pattern; (b) Bright field TEM image and experimental SAED of electrode at 0.01 V with indexed $Li_{0.98}MoO_2$ pattern; (c) Bright field TEM image and experimental SAED of electrode at 3 V with indexed MoO_2 pattern; (d) Bright field TEM image and EELS of electrode at 0.01V.

The SEM images shown in Figs 6 offer compelling evidence that supports the formation of a metallic Li layer at the interface. The SEM image depicted in Fig. 6a showcases a lithiated electrode that was immediately transferred to the SEM without any exposure to air. In contrast, Fig. 6b displays the SEM image of the same electrode after it was allowed to remain in air for approximately 10 min. A distinct difference can be observed: in Fig. 6b, there is a visible gel-coating like fusion among particles, which is absent in Fig. 6a. This observable fusion in Fig. 6b can likely be attributed to the reaction between the Li-rich layer on the particle surface and the ambient air. More SEM images comparison displayed in Fig. S6. Further insights from the EDX mapping analysis, as shown in Fig. 6c and d, reveal that a significant portion of oxygen is distributed across the particle surface, diverging from the distribution pattern of Mo. Moreover, the oxygen-to-molybdenum ratio is considerably higher when compared to the electrode that was

not exposed to air. This rapid absorption of oxygen from the air strongly indicates the existence of a Li layer enveloping the particles. It also suggests that the conversion reaction did not happen.

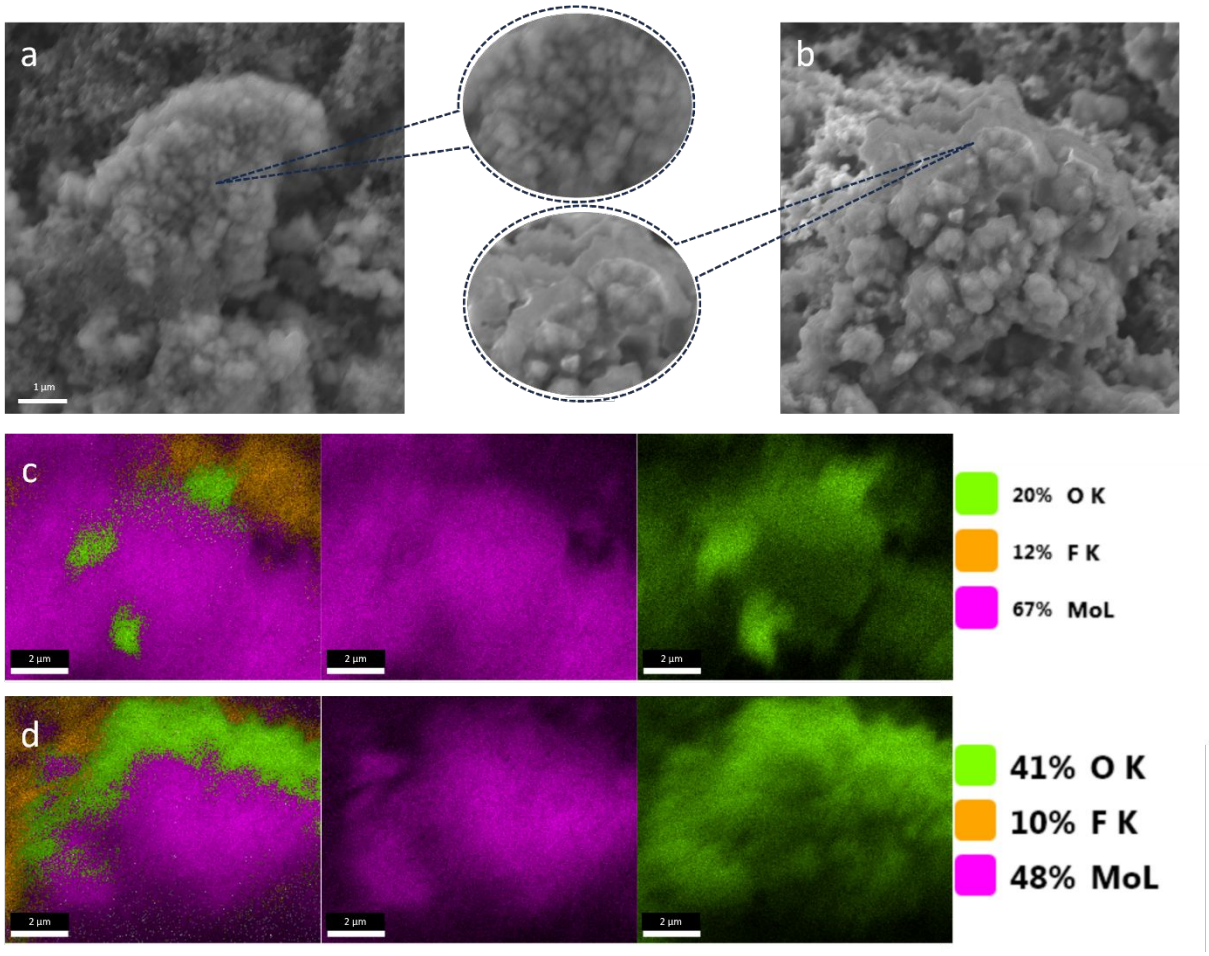

Fig. 6. SEM images and EDX mapping of lithiated MoO_2 electrodes. (a) electrode without exposure to air; (b) electrode exposed to air; (c) electrode without exposed to air and (d) electrode exposed to air.

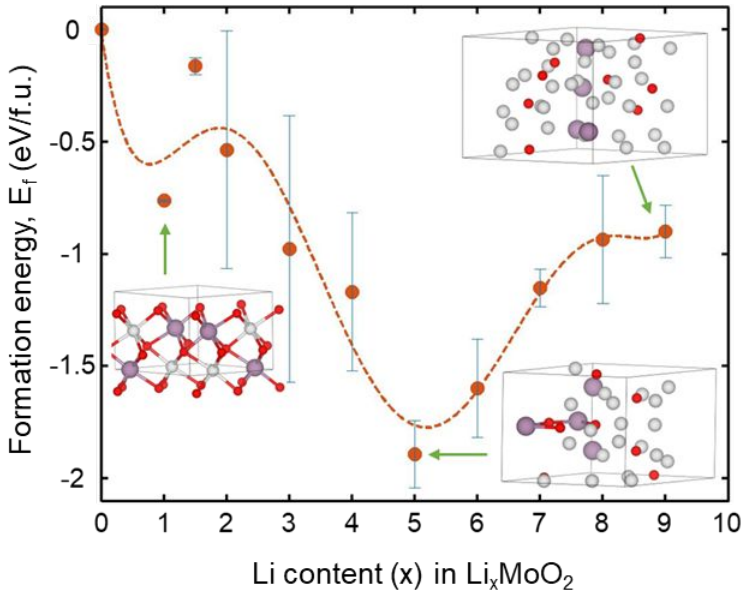

Fig. 7. Variation in the predicted formation energy (E_f) of lithiated MoO_2 (Li_xMoO_2) as a function of Li content (x). Insets show $LiMoO_2$, Li_5MoO_2, and Li_9MoO_2 structures, as indicated, where purple, red, and white balls represent Mo, O, and Li atoms, respectively. For each composition, three independent samples were considered, where the energy variation is represented by an error bar.

To further understand the Li storage mechanism in Li-rich phases, DFT calculations were performed to determine the structure and energetics of bulk MoO_2 with varying Li content (x) for both crystalline and amorphous phases. Fig. 7 shows the variations in the formation energy (E_f) per formula unit (f. u.) of lithiated MoO_2 (Li_xMoO_2) as a function of x, with respect to crystalline MoO_2 and body-centered cubic Li (*bcc*-Li); the atomic structure of crystalline MoO_2 is shown in the supporting information. Here, E_f is given by:

$$E_f = E_{Lix\mathrm{MoO2}} - E_{\mathrm{MoO2}} - x \times E_{Li}, \qquad (2)$$

where the first and second terms on the right side of equation are the total energies of Li_xMoO_2 and pristine MoO_2 per f.u., respectively, and E_{Li} is the per-atom energy of *bcc*-Li. Li atoms were inserted into the octahedral lattice sites of crystalline MoO_2 to construct crystalline $LiMoO_2$, resulting in a decrease in E_f. The calculation result consists with our experimental observation and previous report, indicating the formation of crystalline lithiation compound.[67] Further insertion of

Li atoms leads to the distortion of the crystalline framework of $LiMoO_2$, while the E_f increases to the local maximum at x = 1.5. With continuous lithiation, the Mo-O matrix undergoes gradual disintegration, ultimately leading to the generation of Mo and Li_2O. E_f is predicted to continuously decrease until it reaches the minimum-energy 'plateau' at x = 5, which is greater than the theoretical estimate of the 'fully lithiated' phase (x = 4). Our results confirm the favorable formation of $LiMoO_2$ in the lithiation map and also provide a theoretical prediction for the possible overlithiated behavior of MoO_2 (in which Li_5MoO_2 can be the most energetically favorable phase).

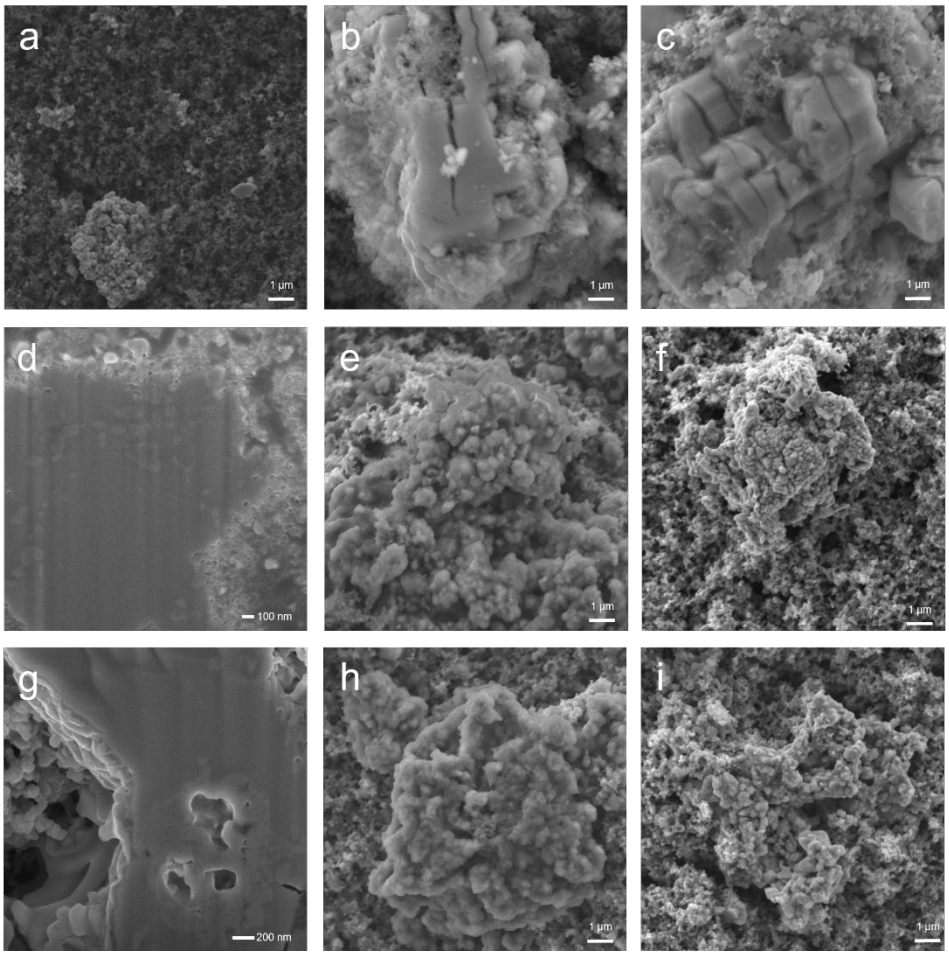

Fig. 8. *Ex-situ* SEM of electrodes. (a) SEM of the pristine electrode; (b) SEM image of the electrode at point 1 after lithiation; (c) SEM image of the electrode at point 1 after delithiation; (d)

SEM image of the cross-section of a lithiated particle at point 1; (e) SEM image of the electrode between points 2 and 3 after lithiation; (f) SEM image of the electrode between points 2 and 3 after delithiation; (g) SEM image of the cross-section of a delithiated particle at point 1; (h) SEM image of the electrode between points 3 and 4 after lithiation; (i) SEM image of the electrode between points 3 and 4 after delithiation.

To investigate the W-shaped capacity variation upon cycling, a series of *ex-situ* SEM and TEM experiments were undertaken. Fig. 8 presents the *ex-situ* SEM images of the electrodes at various stages of cycling. In Figs 8a through 8c, it can be observed that the MoO_2 nanoparticles have a tendency to coalesce into larger aggregates during the initial cycle. Fig. S7 presents a large-scale SEM image of the lithiated electrode at point (1), which clearly illustrates that MoO2 nanoparticles coalesced into larger aggregates and the particle sizes have predominantly grown to the micron scale. This phenomenon is likely to contribute to the capacity decline between points (1) and (2). Subsequently, the aggregated particles that formed during the first cycle undergo a reduction in size as a consequence of volume changes. This is evident in Figs 8c, 8e, 8f, 8h, and 8i. In addition, Figs 8d and 8g depict SEM images of the cross-sections of both lithiated and delithiated bulk particles, respectively, during the initial cycle. The cross-sectional representations reveal the emergence of pores as the cycling progresses. As the particle size diminishes, there is a facilitation in the intercalation reaction and the formation of Li-rich phases, particularly at a high rate (1C). Moreover, the fracturing of larger particles exposes fresh surfaces to the electrolyte, leading to the creation of a new SEI layer. This, in turn, correlates with a relatively lower Coulombic efficiency. Video S1 further illustrates that the peaks associated with intercalation progressively diminish upon cycling and are entirely absent post point (4). This is indicative of a capacity loss ascribable to the waning intercalation reaction. Between points (2) and (3), there is a capacity augmentation, likely attributable to enhanced kinetics and a predominant SEI reaction, which compensates for the capacity reduction caused by the diminished intercalation reaction. Beyond point (3), as depicted in Fig. 1a and Video S1, there is a notable decline in the SEI peak, concurrent with an increase in CE. The capacity reduction during this phase can be potentially ascribed to three underlying mechanisms: (1) The thickening of the SEI layer, which could impede the kinetics. (2) A combined effect of the decreasing particle size and thickening SEI layers could result in a more stable SEI layer as the particles undergo substantial volume changes. This stability leads to a

decrease in discharge capacity attributed to SEI formation, and a subsequent increase in CE, as illustrated in Fig. 1a and Video S1. (3) There is a continued decline in the capacity of the intercalation reaction.

To investigate the alterations in the thickness of the SEI, AC impedance measurements of coin cells at various stages were performed. As depicted in Fig. 9, there is a discernible escalation in the resistance of the SEI from point (2) to point (4). Specifically, the SEI resistance increases from 11.71 Ω at the 2nd cycle to 23.92 Ω at the 46th cycle. The correlated TEM images, which display the SEI thickness, are presented in Fig. S8. In these images, regions containing fluoride and oxygen, but devoid of molybdenum, are identified as SEI. At point (1), the SEI thickness measures approximately 5 to 10 nm and exhibits an increase to around 20 nm at point (4) with continued cycling. Interestingly, subsequent to point (4), the SEI resistance exhibits a declining trend, falling to 4.66 Ω at the 246th cycle and continuing to marginally decrease to 4.51 Ω at the 372nd cycle. This fluctuation in the SEI resistance may suggest alterations in the SEI's formation over the cycles. Initially, between points (1) and (4), the SEI undergoes formation and thickening, which coincides with a lower CE. Following this phase, the SEI transitions to a stable state, and its resistance decreases, potentially due to the increased surface area of the active materials.

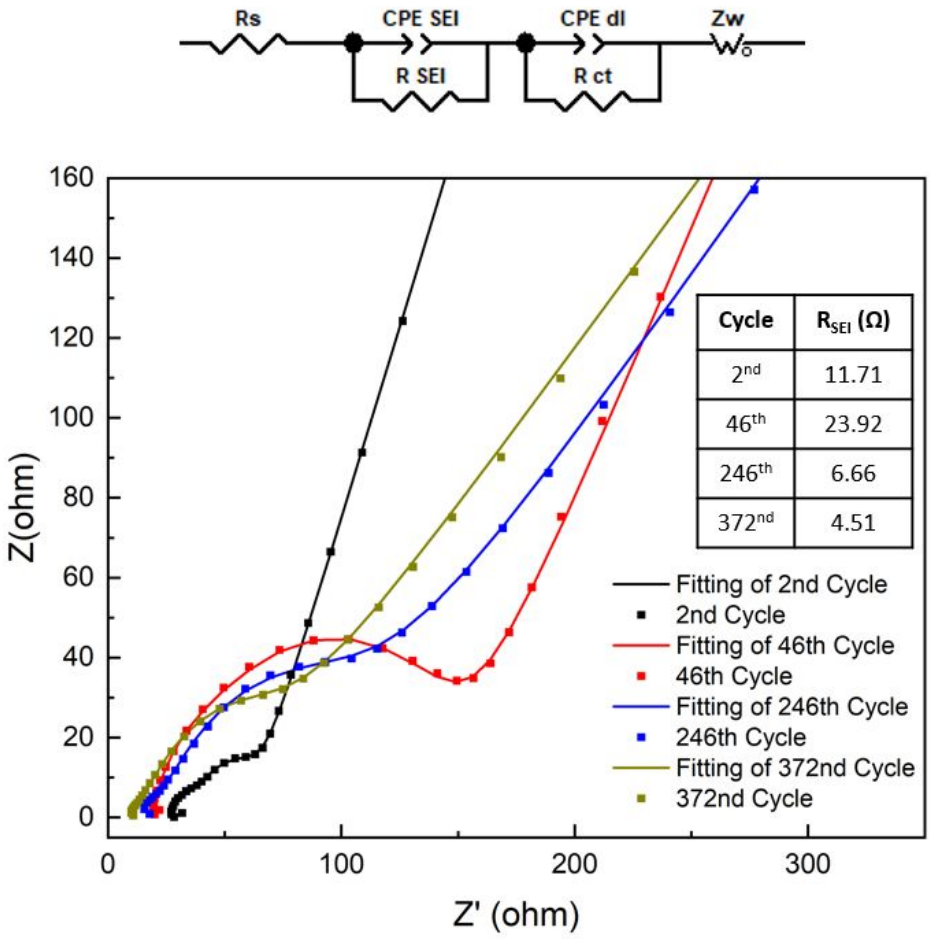

Fig. 9. The equivalent circuit model for EIS fitting, Nyquist plots of a Li//MoO_2 cell at different cycling states, and fitting results of SEI resistance.

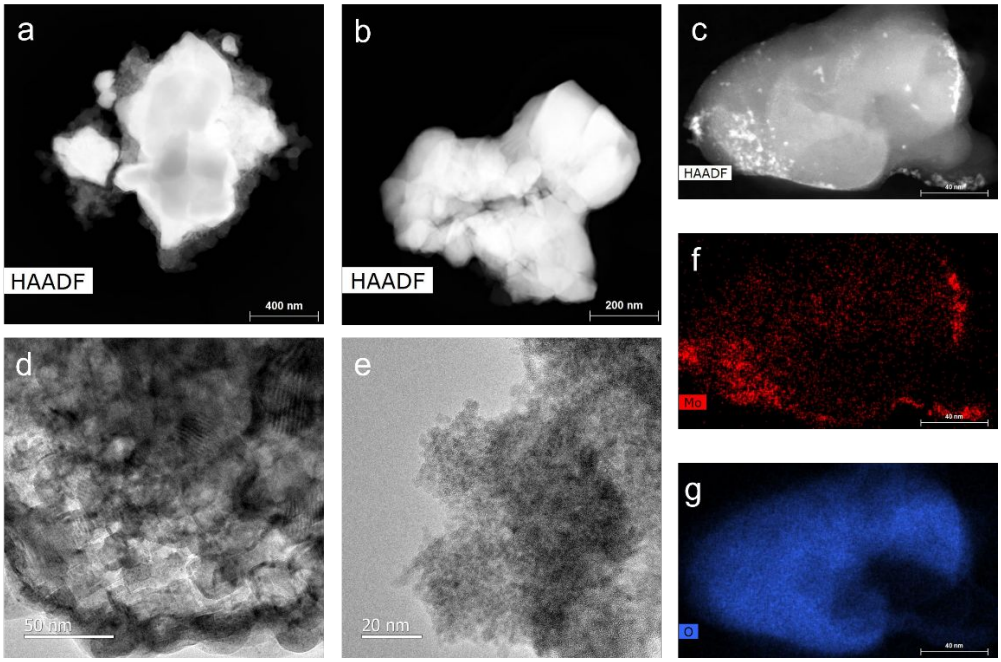

Fig. 10. (a) STEM image of electrode at point (1); (b) STEM image of electrode at point (2); (c) STEM image of electrode at point (4); (d) TEM micrograph of pristine particle; (e) TEM micrograph of particle at point (5); (f), (g) EDX mapping of Mo and oxygen of particle showing in image (c).

The TEM images presented in Fig. 10 depict the evolution of the structure of MoO_2 particles during cycling. Specifically, Fig. 10d reveals that the pristine MoO_2 particle exhibits a polycrystalline structure. As we move to Fig. 10a and b, a notable transformation occurs, with the particle undergoing pulverization and the development of pores. Furthermore, Fig. 10c and e demonstrate a transition of the particle into atomic clusters once the capacity surpasses the theoretical limit, occurring between points (4) and (5). There is also the presence of nanometer-sized MoO_2 particles, manifested as bright white spots in Fig. 10c, which are expected to further pulverize into atomic clusters upon subsequent cycling. In addition, Fig. 1a highlights that the capacity experiences a continuous increment, while the Coulombic efficiency remains nearly stable after reaching the threshold between points (4) and (5). This rise in capacity can be attributed to the escalation in surface area resulting from the particles' pulverization. To add to this, a $LiMoO_2$ slab was constructed to illustrate the impact of surface on the displayed capacity. As shown in Fig. 11, Li atoms were added onto the surface of $LiMoO_2$ while keeping its inner crystalline framework intact, mimicking the finding that $LiMoO_2$ is metastable upon the course of lithiation. The

deposition of a Li monolayer tends to stabilize the $LiMoO_2$ surface by saturating the surface O atoms. The E_f of the Li monolayer is predicted to be -0.93 eV/atom; the sizable negative value implies that the formation of a Li rich phase on the surface of $LiMoO_2$ would be energetically favorable. The excess Li atoms accumulated on the surface can be readily stripped during the discharge process, which may in turn significantly contribute to the extra capacity of $LiMoO_2$. These simulation results provide strong support for our experimental observations concerning the origin of the extra capacity for $LiMoO_2$. This finding highlights the importance of considering surface phenomena when describing and understanding the electrochemical behavior of the MoO_2 anode.

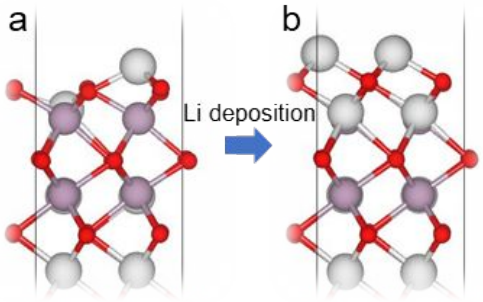

Fig. 11. Atomic structure of (a) $LiMoO_2$ slab structure and (b) with 1 monolayer of Li atoms.

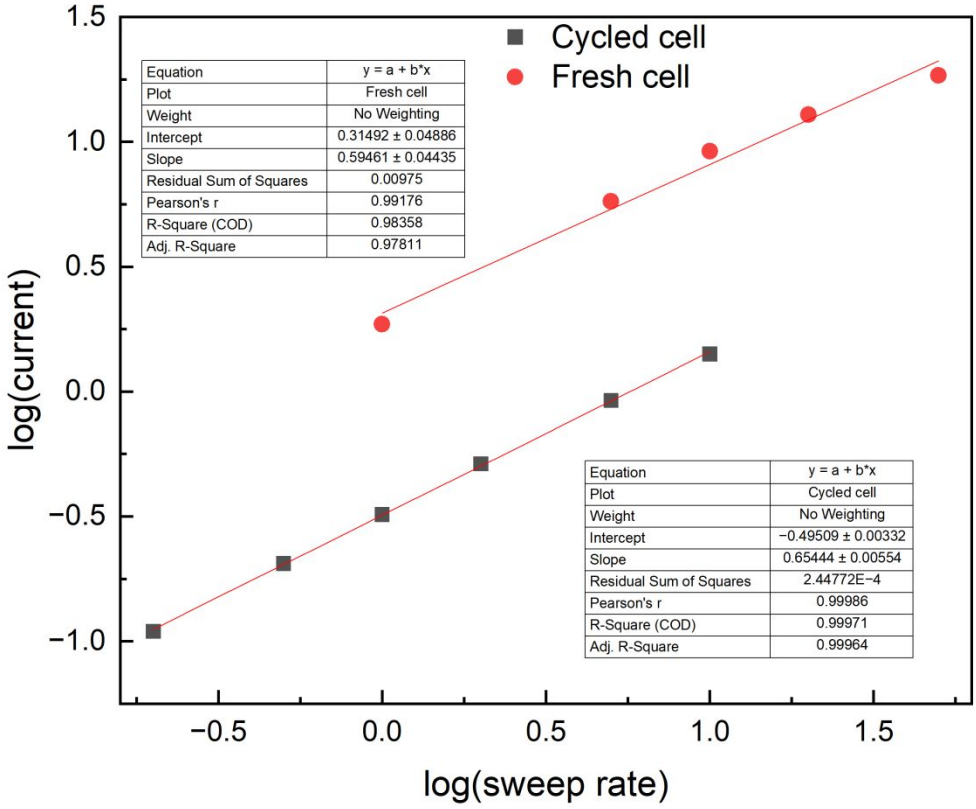

Fig. 12. Linear fitting of log(current) *vs*. log (sweep rate)

Fig. 12 illustrates the linear fit that depicts the relationship between the current and the sweep rate, which were obtained in a series of CV experiments with different scanning ~~current~~ rates. By employing cyclic voltammetry with varying sweep rates, it is possible to analyze both the Faradaic and the capacitive effects. The contribution of capacitance to the total charge storage can be bifurcated into two components, namely, the surface capacitive contribution and the contribution from the diffusion-controlled process. This relationship is represented by the equation:

$$i = av^b, \qquad (3)$$

where i represents the measured current, while v denotes the sweep rate. a and b are adjustable parameters, with the value of b being ascertainable through the slope of the linear fit of log (i) versus log (v)). There are two well-defined conditions when $b = 0.5$ or 1. When $b = 0.5$, the

current is governed by diffusion, and is proportional to the square root of the sweep rate, according to the following equation:

$$i = nFAC^{*} D^{\frac{1}{2}} v^{\frac{1}{2}} \left(\frac{\alpha nF}{RT}\right)^{\frac{1}{2}} \pi^{\frac{1}{2}} x(bt), \quad (4)$$

where C^{*} is the surface concentration of the electrode material, R is the transfer coefficient, D is the chemical diffusion coefficient, n is the number of electrons involved in the electrode reaction, A is the surface area of the electrode materials, F is the Faraday constant, R is the molar gas constant, T is the temperature, and the $x(bt)$ function represents the normalized current for a totally irreversible system as indicated by the cyclic voltammetry.

When $b = 1$ the current is governed by the capacitive response on the surface and is proportional to the sweep rate, according to the following equation:

$$i = vC_d A, \quad (5)$$

where C_d is the capacitance.[68-70] As per the results derived from our linear fitting, the value of b escalated to approximately 0.65 following extensive cycling, up from roughly 0.59 in the fresh state. This surge in the capacitive effect implies an increase in the surface area post-cycling, which aligns with our analysis of capacity variation.

Beyond point (5), the capacity exhibits inconsistencies, largely attributed to detachment stemming from volumetric changes. Addressing this can potentially involve adopting meticulous nanostructure designs, like mesoporous nanoparticles or two-dimensional nanosheets. [15, 45, 54] Such configurations would not only maximize the immediate benefits of the additional capacity (originating from the lithium-rich layer) due to their expansive surface area, but also ensure sustained high capacity across prolonged cycling durations.

4. Conclusion

This research examined the capacity variation upon cycling of MoO_2 nanoparticles as well as the underlying mechanisms responsible for its remarkable excess capacity, which transcends the theoretical limit based on conversion reactions. Through *in-situ* XRD and XAS analyses, coupled with SAED patterns, we have ascertained that MoO_2 undergoes a Li-ion intercalation during the discharging process without necessitating any subsequent conversion reaction to yield Mo and Li_2O. Furthermore, the EELS and EDX assessments of the lithiated electrode offer evidence to propose that the extra capacity is attributable to the formation of a metallic, Li-rich phase

subsequent to the Li ion intercalation, which plays an instrumental role in Li storage. Moreover, the *ex-situ* SEM, TEM, and EIS analyses shed light on the intricate interplay between particle size, morphology, surface characteristics, and the formation of SEI, elucidating the intriguing W-shaped capacity variation upon cycling. In summary, these findings provide a foundation for the development of high-capacity anode materials for LIBs.

Acknowledgments

This article was derived from the subject data funded in part by the United States Agency for International Development (USAID) and the National Academy of Sciences (NAS) through Subaward 2000010562. Any opinions, findings, conclusions, or recommendations expressed in this article are those of the authors alone and do not necessarily reflect the views of USAID or NAS. The Egyptian authors are grateful for the financial support from the Science, Technology, and Innovation Funding Authority (STIFA, STDF previously) through project number 42691 entitled "Microstructure-Based, Multi-Physics Simulation and Optimization to Improve Battery Performance". Work performed at the Center for Nanoscale Materials and Advanced Photon Source, both U.S. Department of Energy Office of Science User Facilities, was supported by the U.S. DOE, Office of Basic Energy Sciences, under Contract No. DE-AC02-06CH11357.

References

1. Y. Nishi, *Chem Rec*, 2001, **1**, 406-413.
2. Y. M. Sun, N. A. Liu and Y. Cui, *Nat Energy*, 2016, **1**.
3. B. L. Ellis, K. T. Lee and L. F. Nazar, *Chem Mater*, 2010, **22**, 691-714.
4. T. Zheng and J. Dahn, *Carbon Materials for Advanced Technologies*, Pergamon, 1999.
5. K. Z. Cao, T. Jin, L. Yang and L. F. Jiao, *Materials Chemistry Frontiers*, 2017, **1**, 2213-2242.
6. H. B. Wu, J. S. Chen, H. H. Hng and X. W. Lou, *Nanoscale*, 2012, **4**, 2526-2542.
7. M. V. Reddy, T. Yu, C. H. Sow, Z. X. Shen, C. T. Lim, G. V. S. Rao and B. V. R. Chowdari, *Advanced Functional Materials*, 2007, **17**, 2792-2799.
8. L. Zhang, H. B. Wu and X. W. Lou, *Advanced Energy Materials*, 2014, **4**.
9. A. Kraytsberg and Y. Ein-Eli, *Journal of Solid State Electrochemistry*, 2017, **21**, 1907-1923.
10. S. Fang, D. Bresser and S. Passerini, *Advanced Energy Materials*, 2020, **10**.
11. Y. Lu, Y. Yu and X. W. Lou, *Chem*, 2018, **4**, 972-996.
12. J. M. Tarascon and M. Armand, *Nature*, 2001, **414**, 359-367.
13. S. H. Yu, S. H. Lee, D. J. Lee, Y. E. Sung and T. Hyeon, *Small*, 2016, **12**, 2146-2172.

14. P. Poizot, S. Laruelle, S. Grugeon, L. Dupont and J. M. Tarascon, *Nature*, 2000, **407**, 496-499.
15. J. K. Shon, H. S. Lee, G. O. Park, J. Yoon, E. Park, G. S. Park, S. S. Kong, M. Jin, J. M. Choi, H. Chang, S. Doo, J. M. Kim, W. S. Yoon, C. Pak, H. Kim and G. D. Stucky, *Nat Commun*, 2016, **7**.
16. S. Laruelle, S. Grugeon, P. Poizot, M. Dolle, L. Dupont and J. M. Tarascon, *Journal of the Electrochemical Society*, 2002, **149**, A627-A634.
17. G. M. Zhou, D. W. Wang, F. Li, L. L. Zhang, N. Li, Z. S. Wu, L. Wen, G. Q. Lu and H. M. Cheng, *Chem Mater*, 2010, **22**, 5306-5313.
18. S. K. Behera, *Chem Commun*, 2011, **47**, 10371-10373.
19. C. M. Ban, Z. C. Wu, D. T. Gillaspie, L. Chen, Y. F. Yan, J. L. Blackburn and A. C. Dillon, *Adv Mater*, 2010, **22**, E145-+.
20. S. Chaudhari and M. Srinivasan, *J Mater Chem*, 2012, **22**, 23049-23056.
21. S. L. Chou, J. Z. Wang, D. Wexler, K. Konstantinov, C. Zhong, H. K. Liu and S. X. Dou, *J Mater Chem*, 2010, **20**, 2092-2098.
22. C. X. Peng, B. D. Chen, Y. Qin, S. H. Yang, C. Z. Li, Y. H. Zuo, S. Y. Liu and J. H. Yang, *Acs Nano*, 2012, **6**, 1074-1081.
23. Y. M. Sun, X. L. Hu, W. Luo and Y. H. Huang, *J Mater Chem*, 2012, **22**, 13826-13831.
24. X. H. Wang, X. W. Li, X. L. Sun, F. Li, Q. M. Liu, Q. Wang and D. Y. He, *J Mater Chem*, 2011, **21**, 3571-3573.
25. Y. M. Sun, X. L. Hu, W. Luo and Y. H. Huang, *J Mater Chem*, 2012, **22**, 19190-19195.
26. W. X. Zhang, M. Li, Q. Wang, G. D. Chen, M. Kong, Z. H. Yang and S. Mann, *Adv Funct Mater*, 2011, **21**, 3516-3523.
27. Y. Chen, B. H. Song, X. S. Tang, L. Lu and J. M. Xue, *J Mater Chem*, 2012, **22**, 25496-25496.
28. S. L. Jin, H. G. Deng, D. H. Long, X. J. Liu, L. A. Zhan, X. Y. Liang, W. M. Qiao and L. C. Ling, *J Power Sources*, 2011, **196**, 3887-3893.
29. S. M. Yuan, J. X. Li, L. T. Yang, L. W. Su, L. Liu and Z. Zhou, *Acs Applied Materials & Interfaces*, 2011, **3**, 705-709.
30. L. W. Su, Y. R. Zhong and Z. Zhou, *J Mater Chem A*, 2013, **1**, 15158-15166.
31. S. Grugeon, S. Laruelle, R. Herrera-Urbina, L. Dupont, P. Poizot and J. M. Tarascon, *J Electrochem Soc*, 2001, **148**, A285-A292.
32. S. Grugeon, S. Laruelle, L. Dupont and J. M. Tarascon, *Solid State Sci*, 2003, **5**, 895-904.
33. H. Li, G. Richter and J. Maier, *Advanced Materials*, 2003, **15**, 736-739.
34. J. Jamnik and J. Maier, *Physical Chemistry Chemical Physics*, 2003, **5**, 5215-5220.
35. H. Li, P. Balaya and J. Maier, *Journal of the Electrochemical Society*, 2004, **151**, A1878-A1885.
36. J. Maier, *Faraday Discussions*, 2007, **134**, 51-66.
37. Y. F. Zhukovskii, P. Balaya, E. A. Kotomin and J. Maier, *Physical Review Letters*, 2006, **96**.
38. Q. Li, H. S. Li, Q. T. Xia, Z. Q. Hu, Y. Zhu, S. S. Yan, C. Ge, Q. H. Zhang, X. X. Wang, X. T. Shang, S. T. Fan, Y. Z. Long, L. Gu, G. X. Miao, G. H. Yu and J. S. Moodera, *Nature Materials*, 2021, **20**.
39. M. Keppeler and M. Srinivasan, *Chemelectrochem*, 2017, **4**, 2727-2754.
40. G. X. Wang, H. Liu, J. Horvat, B. Wang, S. Z. Qiao, J. Park and H. Ahn, *Chem-Eur J*, 2010, **16**, 11020-11027.

41. B. Liu, X. L. Hu, H. H. Xu, W. Luo, Y. M. Sun and Y. H. Huang, *Sci Rep-Uk*, 2014, **4**.
42. J. C. Guo, Q. Liu, C. S. Wang and M. R. Zachariah, *Adv Funct Mater*, 2012, **22**, 803-811.
43. W. Luo, X. L. Hu, Y. M. Sun and Y. H. Huang, *Acs Applied Materials & Interfaces*, 2013, **5**, 1997-2003.
44. B. Sun, J. Horvat, H. S. Kim, W. S. Kim, J. Ahn and G. X. Wang, *J Phys Chem C*, 2010, **114**, 18753-18761.
45. C. Xia, Y. G. Zhou, D. B. Velusamy, A. A. Farah, P. Li, Q. Jiang, I. N. Odeh, Z. G. Wang, X. X. Zhang and H. N. Alshareef, *Nano Lett*, 2018, **18**, 1506-1515.
46. Z. L. Xiu, D. Kim, M. H. Alfaruqi, J. Song, S. Kim, P. T. Duong, V. Mathew, J. P. Baboo and J. Kim, *J Alloy Compd*, 2017, **696**, 143-149.
47. H. J. Zhang, J. Shu, K. X. Wang, X. T. Chen, Y. M. Jiang, X. Wei and J. S. Chen, *J Mater Chem A*, 2014, **2**, 80-86.
48. L. C. Yang, Q. S. Gao, Y. H. Zhang, Y. Tang and Y. P. Wu, *Electrochem Commun*, 2008, **10**, 118-122.
49. Y. Q. Feng, H. Liu, Y. Liu and J. Q. Li, *Int J Energ Res*, 2022, **46**, 5789-5799.
50. P. Zhang, L. Zou, H. X. Hu, M. R. Wang, J. Fang, Y. Q. Lai and J. Li, *Electrochim Acta*, 2017, **250**, 219-227.
51. L. Chen, H. Jiang, H. B. Jiang, H. X. Zhang, S. J. Guo, Y. J. Hu and C. Z. Li, *Adv Energy Mater*, 2017, **7**.
52. L. C. Yang, X. Li, Y. P. Ouyang, Q. S. Gao, L. Z. Ouyang, R. Z. Hu, J. Liu and M. Zhu, *Acs Applied Materials & Interfaces*, 2016, **8**, 19987-19993.
53. J. Li, H. Wei, F. Hu, Z. Xie, J. P. Hei, Y. Q. Kong, X. J. Yin, N. N. Wang and H. H. Wei, *Int J Hydrogen Energ*, 2022, **47**, 32594-32606.
54. Y. Yao, Z. A. Chen, R. H. Yu, Q. Chen, J. X. Zhu, X. F. Hong, L. Zhou, J. S. Wu and L. Q. Mai, *Acs Applied Materials & Interfaces*, 2020, **12**, 40648-40654.
55. H. Wang, T. Y. Li, A. M. Hashem, A. E. Abdel-Ghany, R. S. El-Tawil, H. M. Abuzeid, A. Coughlin, K. Chang, S. X. Zhang, H. El-Mounayri, A. Tovar, L. K. Zhu and C. M. Julien, *Nanomaterials-Basel*, 2022, **12**.
56. M. Klinger, *J Appl Crystallogr*, 2017, **50**, 1226-1234.
57. G. Kresse and J. Hafner, *Phys. Rev. B*, 1993, **47**, 558.
58. G. Kresse and J. Furthmüller, *Comput. Mater. Sci.*, 1996, **6**, 15-50.
59. G. Kresse and J. Furthmüller, *Phys. Rev. B*, 1996, **54**, 11169.
60. J. P. Perdew, K. Burke and M. Ernzerhof, *Phys. Rev. Lett.*, 1996, **77**, 3865.
61. P. E. Blöchl, *Phys. Rev. B*, 1994, **50**, 17953.
62. H. J. Monkhorst and J. D. Pack, *Phys. Rev. B*, 1976, **13**, 5188.
63. W. Hao, M. Lee and G. S. Hwang, *J. Power Sources*, 2023, **560**, 232689.
64. J. R. Dahn and W. R. Mckinnon, *Solid State Ionics*, 1987, **23**, 1-7.
65. Y. L. Liu, H. Zhang, P. Ouyang, W. H. Chen and Z. C. Li, *Mater Res Bull*, 2014, **50**, 95-102.
66. F. Wang, J. Graetz, M. S. Moreno, C. Ma, L. J. Wu, V. Volkov and Y. M. Zhu, *Acs Nano*, 2011, **5**, 1190-1197.
67. J. K. Shon, H. S. Lee, G. O. Park, J. Yoon, E. Park, G. S. Park, S. S. Kong, M. Jin, J.-M. Choi and H. Chang, *Nature communications*, 2016, **7**, 11049.
68. H. Lindstrom, S. Sodergren, A. Solbrand, H. Rensmo, J. Hjelm, A. Hagfeldt and S. E. Lindquist, *J Phys Chem B*, 1997, **101**, 7717-7722.
69. F. P. Ijsseling, *Brit Corros J*, 1980, **15**, 51-69.

70. J. Wang, J. Polleux, J. Lim and B. Dunn, *J Phys Chem C*, 2007, **111**, 14925-14931.